

Modeling q_{95} Windows for the Suppression of Edge Localized Modes by Resonant Magnetic Perturbations in the DIII-D Tokamak

R. Fitzpatrick^a

*Institute for Fusion Studies, Department of Physics,
University of Texas at Austin, Austin TX, 78712, USA*

A toroidal asymptotic matching model of the response of a tokamak plasma to a static resonant magnetic perturbation (RMP) is used to simulate the $n = 3$ RMP-induced edge-localized-mode (ELM)-suppression windows in q_{95} that are evident when the plasma current is slowly ramped in DIII-D discharge #145380. All quantities employed in the simulation are derived from experimental measurements, apart from the neutral particle data. Three cases are considered. In the first case, the natural frequencies of tearing modes resonant in the plasma are determined by the ion flows at the corresponding resonant surfaces, which is the prediction of nonlinear tearing mode theory. In the second case, the natural frequencies are determined by the local $\mathbf{E} \times \mathbf{B}$ velocities at the resonant surfaces. In the third case, the natural frequencies are determined by the electron flows at the resonant surfaces, which is the prediction of linear tearing mode theory. The second case gives the best agreement between the simulations and the experimental observations. The first and third cases only leads to partial agreement between the simulations and the observations. In the first case, the lack of complete agreement may be a consequence of using an inaccurate assumption for the neutral particle distribution in the pedestal. In the third case, the lack of complete agreement is probably due to the fact that the response of a tokamak plasma to an RMP is not accurately described by linear tearing mode theory.

^a rfitzp@farside.ph.utexas.edu

I. INTRODUCTION

Tokamak discharges operating in high-confinement mode (H-mode)¹ exhibit intermittent bursts of heat and particle transport, emanating from the outer regions of the plasma, that are known as (type-I) “edge localized modes” (ELMs).² It is estimated that the heat load that ELMs will deliver to the tungsten plasma-facing components in a reactor-scale tokamak, such as ITER, will be large enough to cause massive tungsten ion influx into the plasma core, and that the erosion associated with this process will unacceptably limit the lifetimes of these components.³ Consequently, the development of robust and effective methods for ELM control is a high priority for the international magnetic fusion program.

The most promising method for the control of ELMs in H-mode tokamak discharges is via the application of static “resonant magnetic perturbations” (RMPs). Complete RMP-induced ELM suppression was first demonstrated on the DIII-D tokamak.⁴ Subsequently, either mitigation or complete suppression of ELMs has been demonstrated on the JET,⁵ ASDEX-U,⁶ KSTAR,⁷ MAST⁸, and EAST⁹ tokamaks.

The application of a static RMP, resonant in the pedestal region (i.e., the region of strong pressure and current density gradients characteristic of the edge region of an H-mode tokamak discharge), to an H-mode tokamak discharge is observed to give rise to two distinct phenomena.^{10–15} The first of these is the so-called “density pump-out”, which is characterized by a reduction in the electron number density in the pedestal region that varies smoothly with the amplitude of the applied RMP, is (usually) accompanied by a similar, but significantly smaller, reduction in the electron and ion temperatures, but is not associated with ELM suppression. The second phenomenon is “ELM suppression” itself, which occurs when the amplitude of the applied RMP exceeds a certain threshold value. ELM suppression is only observed to take place when q_{95} (i.e., the safety-factor on the magnetic flux-surface that encloses 95% of the poloidal flux enclosed by the last closed flux-surface) takes values that lie in certain narrow windows.^{13,15}

Numerical simulations made using the cylindrical, nonlinear, two-fluid, reduced-magneto-hydrodynamical (MHD), initial-value code, TM1^{16–18} have shed considerable light on the hitherto poorly understood physical mechanism that underlies RMP-induced ELM suppression in H-mode tokamak discharges.¹⁹ The simulations in question make a plausible case that the density pump-out phenomenon is associated with the formation of locked (i.e.,

non-rotating) helical magnetic island chains at the bottom of the pedestal, whereas the ELM-suppression phenomenon is associated with the formation of a locked helical magnetic island chain at the top of the pedestal. The prevailing hypothesis is that such an island chain suppresses ELMs by limiting the radial expansion of the pedestal, and, thereby, preventing it from attaining a width sufficient to destabilize peeling-ballooning modes²⁰ (which are thought to trigger ELMs).²¹

Recently, a toroidal generalization of the cylindrical asymptotic matching model presented in Ref. 22 was formulated and used to model RMP-induced ELM-suppression experiments performed on the DIII-D tokamak,²³ leading to similar conclusions to the aforementioned TM1 studies. The first aim of this paper is to employ this new model to try to account for the q_{95} ELM-suppression/mitigation windows that are apparent when the edge safety-factor is slowly ramped in a particular DIII-D discharge (#145380) in which an $n = 3$ RMP is used to control ELMs.^{21,24} The second aim is to determine which choice for the so-called “natural frequency” of tearing modes can best account for the q_{95} ELM-suppression/mitigation windows observed in DIII-D discharge #145380.

II. NATURAL FREQUENCY

A. Introduction

It is well-known that magnetic reconnection driven when a (stable) tearing mode interacts with a static RMP that is resonant at a particular magnetic flux-surface in a tokamak plasma is facilitated when the associated natural frequency, in the absence of the RMP, is relatively small.^{25,26} The natural frequency of a (stable) tearing mode is the helical phase velocity that the mode would possess were it naturally unstable. (It should be noted that the maximum practical currents that can be driven in edge-resonant RMP coils severely limit the ability of such coils to modify the rotation frequencies of tearing modes resonant in the pedestals of present-day tokamaks. For example, in the DIII-D tokamak, as will become clear later on in the paper, the RMP coils are only capable of arresting the rotation of edge-resonant tearing modes when the magnitude of the helical phase velocities of such modes fall below about 5 krad/s. A typical phase velocity is 100 krad/s.) Driven magnetic reconnection leads to the formation of a locked magnetic island chain at the resonant surface in question. Hence,

the prevailing hypothesis is that a q_{95} window for RMP-induced ELM suppression occurs when q_{95} is such that the natural frequency of a tearing mode resonant at the top of the pedestal is close to zero.²¹ However, there is currently some debate in the fusion community regarding the appropriate choice for the natural frequency.

The natural frequency of a tearing mode is determined by the equilibrium plasma flow at the resonant surface. Now, a magnetic island chain is a helical pattern in the magnetic field generated by a helical current perturbation that is localized in the vicinity of the resonant surface. Given that plasma current is predominately carried by the electrons, it is natural to suppose that a magnetic island chain (as well as the tearing mode perturbation away from the resonant surface) is convected by the electron fluid in the immediate vicinity of the resonant surface. This is indeed the case in the linear regime.²⁷ Of course, as a consequence of diamagnetic flows, if the island chain is convected by the electron fluid at the resonant surface then it propagates with respect to the local ion fluid. However, this is not a problem because a linear layer is sufficiently thin that the magnetic field can diffuse through the plasma very rapidly, which implies that the ion fluid is not tied to the magnetic structure of the island chain.

The situation is very different in the nonlinear regime. The region inside the magnetic separatrix of a nonlinear magnetic island chain is governed by a combination of flux-freezing and perturbed force balance. This implies that both the electron and the ion fluids are trapped inside the separatrix, and are, therefore, forced to co-rotate with the island chain. There is no such constraint outside the separatrix, so the electron and ion fluids rotate at different speeds in this region, as a consequence of diamagnetism. It follows that one or other of the electron and the ion fluid rotation profiles must exhibit a strong gradient across the separatrix. The island propagation velocity is determined by which of the two fluids is most resistant to the formation of such a gradient. Of course, it is the ion fluid which is more resistant because of its much greater perpendicular viscosity,^{28,29} as well as its much larger neoclassical stress tensor.³⁰ Hence, a nonlinear magnetic island chain is convected by the ion fluid in the vicinity of the resonant surface, because this choice of propagation speed minimizes the ion fluid velocity gradient across the separatrix.

Finally, we could imagine that if the width of an island chain is neither much less than the linear layer width (which is the strict criterion for the validity of linear theory) nor much greater than the linear layer width (which is the strict criterion for the validity of nonlinear

theory) then the chain lies in some sort of intermediate regime in which it is convected at the local $\mathbf{E} \times \mathbf{B}$ velocity (this prediction is generally intermediate between the predictions of linear and nonlinear theory).

It is clear, from the preceding discussion, that there are three main choices for the natural frequency of a given tearing mode in a tokamak plasma.

B. Case 1

As we have already mentioned, according to nonlinear tearing mode theory, a tearing mode is essentially convected by the local ion fluid at the resonant surface.^{28,30,31} In fact, if the response of an H-mode tokamak plasma to an applied RMP is governed by nonlinear physics then we would expect the natural frequency to take the form²³

$$\varpi_{\perp i} = -n \left(\omega_E + \left[1 - L_{00}^{ii} + L_{01}^{ii} \left(\frac{\eta_i}{1 + \eta_i} \right) \right] \omega_{*i} - \left[L_{00}^{iI} - L_{01}^{iI} \left(\frac{\eta_I}{1 + \eta_I} \right) \right] \omega_{*I} \right), \quad (1)$$

where

$$\omega_E(\Psi_p) = -\frac{d\Phi}{d\Psi_p}, \quad (2)$$

$$\omega_{*a}(\Psi_p) = -\frac{T_a}{Z_a e} \frac{d \ln p_a}{d\Psi_p}, \quad (3)$$

$$\eta_a(\Psi_p) = \frac{d \ln T_a}{d \ln n_a}, \quad (4)$$

for $a = i, I$. Here, e is the magnitude of the electron charge, Ψ_p the equilibrium poloidal magnetic flux (divided by 2π), $\Phi(\Psi_p)$ the equilibrium scalar electric potential, and n the toroidal mode number of the RMP. Moreover, Z_i , $n_i(\Psi_p)$, $T_i(\Psi_p)$, and $p_i(\Psi_p) = n_i T_i$ are the charge number, equilibrium number density, equilibrium temperature, and equilibrium pressure of the majority (thermal) ions, respectively, whereas Z_I , n_I , T_I , $p_I = n_I T_I$ are the corresponding quantities for the impurity ions. Furthermore, $L_{00}^{ii}(\Psi_p)$, $L_{01}^{ii}(\Psi_p)$, $L_{00}^{iI}(\Psi_p)$, and $L_{01}^{iI}(\Psi_p)$ are neoclassical parameters that are defined in Sect. B of Ref. 23. Note that these parameters are affected by charge exchange with neutrals. The right-hand side of Eq. (1) is evaluated at the “rational” (i.e., resonant) magnetic flux-surface at which the safety-factor,

$$q(\Psi_p) = \frac{d\Psi_t}{d\Psi_p}, \quad (5)$$

takes the rational value m/n , where m is a positive integer. Here, m and n are the numbers of poloidal and toroidal periods, respectively, of the helical magnetic island chain driven at

the rational surface. Moreover, $\Psi_t(\Psi_p)$ is the equilibrium toroidal (poloidal) magnetic flux (divided by 2π).

C. Case 2

A second possibility is that a tearing mode is convected at the local $\mathbf{E} \times \mathbf{B}$ velocity at the resonant surface,^{14,15,32} in which case we would expect the natural frequency to take the form

$$\varpi_{\perp EB} = -n \omega_E. \quad (6)$$

As before, the right-hand side of Eq. (6) is evaluated at the rational magnetic flux-surface.

D. Case 3

Finally, according to linear tearing mode theory, a tearing mode is essentially convected by the local electron fluid at the resonant surface.^{33,34} Hence, if the response of an H-mode tokamak plasma to an applied RMP is governed by linear physics then we would expect the natural frequency to take the form^{35–37}

$$\varpi_{\perp e} = -n (\omega_E + \omega_{*e}), \quad (7)$$

where

$$\omega_{*e}(\Psi_p) = \frac{T_e}{e} \frac{d \ln p_e}{d \Psi_p}. \quad (8)$$

Here, $p_e(\Psi_p)$ is the equilibrium electron pressure, and $T_e(\Psi_p)$ the equilibrium electron temperature. Finally, as before, the right-hand side of Eq. (7) is evaluated at the rational magnetic flux-surface.

III. EPEC MODELING OF DIII-D DISCHARGE #145380

A. EPEC Code

The theoretical model of the response of a tokamak plasma to an externally applied RMP that is used in this paper is described in detail in Ref. 23. The model employs a

standard asymptotic matching approach.^{27,38–48} According to this approach, the response of the plasma to the applied RMP is governed by a combination of flux-freezing and perturbed force balance (this combination is often referred to as “marginally-stable ideal-MHD”) everywhere in the plasma apart from a number of relatively narrow (in the radial direction) regions in which the applied perturbation resonates with the equilibrium magnetic field. Magnetic reconnection can take place within the resonant regions to produce relatively thin magnetic islands. Within the resonant regions, the plasma response is governed by nonlinear, as opposed to linear, two-fluid resistive-MHD. This is the case because the widths of the magnetic island chains driven at the resonant surfaces (in DIII-D discharge 158115,²² which is similar to DIII-D discharge 145380) exceed the linear layer widths (which invalidates linear theory). (This state of affairs can be expected to persist in future tokamaks, such as ITER, because such tokamaks will operate with much higher values of the Lundquist number than present-day tokamaks, leading to a reduction in the linear layer widths.) Thus, when employing the asymptotic matching approach, the equations of flux-freezing and perturbed force balance are solved in the so-called “outer region” that comprises most of the plasma (and the surrounding vacuum), the equations of nonlinear two-fluid resistive-MHD are solved in the various resonant layers that constitute the so-called “inner region”, and the two sets of solutions are then asymptotically matched to one another.

A toroidal tokamak equilibrium exhibits two distinct types of response to an applied RMP.^{12,49,50} The first of these is known as the “tearing response”—this is a non-ideal-MHD response that is associated with the formation of current sheets and magnetic island chains at various resonant surfaces within the plasma. The second response type is known as the “kink response”—this is an edge-localized ideal-MHD response that is associated with coupling to a stable non-resonant kink mode. For the case of the tearing response, our model employs an approximation in which the plasma response is assumed to be vacuum-like between the various resonant surfaces. On the other hand, the kink response of the plasma is calculated exactly using the GPEC code.^{51,52} (See Sect. A.8 of Ref. 23.)

Our model has been implemented in the newly-developed EPEC (Extended Perturbed Equilibrium Code) code. The name of this code reflects the fact that the nonlinear evolution of tearing modes in a tokamak plasma has far more in common with the $1\frac{1}{2}$ -D evolution of the global plasma equilibrium than it does with conventional linear tearing mode physics. In particular, the Alfvén time is an irrelevant timescale in nonlinear tearing mode theory,

and is also very much shorter than the timescales on which physical quantities of interest actually evolve. (Note that all timescales are normalized to the Alfvén time in Ref. 23. However, this is just a matter of convention. With the benefit of hindsight, it would have been better to normalize the timescales with respect to a diamagnetic timescale, in which case the Alfvén time would have completely dropped out of the final system of equations. See Sect. E in Ref. 23.)

B. Plasma Equilibrium

DIII-D discharge #145380 is an ITER-Similar-Shape (ISS), ELMing, H-mode discharge, with a toroidal magnetic field $B_T = -1.9$ T, in which the plasma current, I_p , is slowly ramped over a 2 second interval in order to scan the magnetic safety-factor.^{21,24} The majority ions are Deuterium, whereas the minority ions are Carbon VI. Figure 1 gives an overview of DIII-D discharge #145380. A static RMP is applied to the plasma by running steady $n = 3$ currents through the I-coil system.⁵³ Three windows of ELM suppression or mitigation are evident: the first (in which ELMs are mitigated, but not entirely suppressed) extends from $t = 2840$ – 2980 ms; the second (in which ELM are entirely suppressed) extends from $t = 3320$ – 3560 ms; and the third (in which ELMs are entirely suppressed) extends from $t = 3880$ – 4200 ms.

Figure 2 shows the measured plasma equilibrium at the start of the current ramp ($t = 2500$ ms). Likewise, Fig. 3 shows the measured plasma profiles at the start of the current ramp. Here, Ψ_N is a normalized equilibrium poloidal magnetic flux defined such that the magnetic axis corresponds to $\Psi_N = 0$, and the last closed magnetic flux-surface (LCFS) to $\Psi_N = 1$. The perpendicular diffusivity data comes from TRANSP modeling.⁵⁴

Measured plasma equilibrium and plasma profiles are reconstructed every 50 ms. The equilibrium and profiles at a given point in time are interpolated from the reconstructed equilibria and profiles. In fact, all quantities that depend on the plasma equilibrium and profiles are recalculated every 1 ms. Data values from the GPEC code are calculated every 100 ms. As before, the GPEC data values at a given point in time are interpolated from the calculated GPEC data values, and any quantity that depends on these values is recalculated every 1 ms. There is one major exception to the aforementioned scheme. The theoretical model implemented in the EPEC code actually requires profiles that are unaffected by the applied RMP (to be more exact, it requires sufficient information to reconstruct natural frequencies

that are unmodified by the electromagnetic torques that develop in the plasma in response to the RMP). However, there is clear evidence that the profiles are significantly modified within the three ELM-suppression/mitigation windows (presumably because wide magnetic island chains are driven in the pedestal). [See Fig. 1(c).] Hence, we do not use the profile (or GPEC) data within the three ELM-suppression/mitigation windows. Instead, we interpolate across these windows using data taken on either side of the windows. The ultimate justification for this approach is the fact that, as can be seen from Figs. 5, 8, and 11, EPEC simulations performed in the absence of the RMP (i.e., in the absence of RMP-generated electromagnetic torques) give very similar natural frequencies to simulations performed in the presence of the RMP, except in time intervals in which one or more tearing modes lock to the RMP (of course, we are identifying such intervals with the ELM suppression/mitigation windows).

Figure 4 shows the safety-factor in DIII-D discharge #145380 as a function of time. It can be seen that $q_{95} \equiv q(\Psi_N = 0.95)$ varies from about 4.1 at the start of the current ramp to about 3.3 at the end. However, the safety-factor at the magnetic axis, $q_0 \equiv q(\Psi_N = 0.0)$, remains approximately constant at about 1.0. For the sake of practicality, the GPEC and EPEC calculations described in this paper ignore $n = 3$ rational surfaces that lie very close to the LCFS; in other words, surfaces that lie in the region $0.997 < \Psi_N \leq 1.000$. (It should be noted that EPEC, like GPEC, employs a straight field-line flux coordinate system, and is effectively spectral in the poloidal and toroidal directions.) $\overline{q_{95}} \equiv 5.2060 - 0.4457 t$ is the least-squares linear fit to the q_{95} versus time data shown in Fig. 4. It follows that the first, second, and third ELM-suppression/mitigation windows extend over the $\overline{q_{95}}$ ranges 3.88–3.94, 3.62–3.73, and 3.33–3.48, respectively.

Note that all quantities used in our theoretical model are derived from experimental measurements taken in DIII-D discharge #145380, with the exception of the neutral particle data. Unfortunately, no neutral particle data is available for DIII-D discharge #145380. Hence, we employ neutral particle data derived from a much earlier discharge (see Sect. III.D of Ref. 23).⁵⁵ In future, data from the new LLAMA (Lyman Alpha Measurement Apparatus) system will be routinely available in DIII-D discharges.⁵⁶ Combining this data with modeling from a neutral particle simulation code, such as, for example, the SOLPS-ITER code,⁵⁷ ought to generate sufficient information to fully determine the neutral particle data required by the EPEC code.

C. Case 1: $\varpi = \varpi_{\perp i}$

The first case that we shall consider is that in which the natural frequency is determined by the local ion fluid; in other words, the natural frequency is specified by Eq. (1).

The upper panel of Fig. 5 shows the natural frequencies, reconstructed by EPEC from profile data, in the absence of the RMP (i.e., in the absence of any RMP-induced electromagnetic torques in the plasma), of the various $n = 3$ tearing modes that are resonant in the pedestal. It can be seen that the natural frequency of the $m = 11$ (brown) tearing mode has its main zero-crossing in the middle of the first ELM-suppression/mitigation window. Likewise, the natural frequency of the $m = 10$ (magenta) tearing mode has its main zero-crossing in the middle of the second ELM-suppression/mitigation window. However, the natural frequency of the $m = 9$ (cyan) tearing mode has its main zero-crossing slightly prior to the occurrence of the third ELM-suppression/mitigation window. The lower panel of Fig. 5 shows the natural frequencies, reconstructed by EPEC from profile data, in the presence of the RMP (i.e., modified by the electromagnetic torques that develop in the plasma in response to the RMP), of the various $n = 3$ tearing modes that are resonant in the pedestal. It is apparent that if the magnitude of the natural frequency in the absence of the RMP falls below about 5 krad/s then the associated tearing mode locks to the RMP (i.e., its true natural frequency becomes zero).

The upper panel of Fig. 6 shows the predicted widths of the various vacuum magnetic island chains driven by the applied $n = 3$ RMP in the pedestal region as functions of \overline{q}_{95} . The vacuum island widths are the expected island widths in the absence of any shielding of driven magnetic reconnection due to plasma flow; in other words, they are the widths of the island chains that would be driven if all of the natural frequencies were zero. It can be seen that the driven magnetic island chains extend over most of the pedestal, implying a very significant degradation in pedestal energy and particle confinement due to the expected flattening of the density and temperature profiles across the chains. Moreover, the driven island chains at the bottom of the pedestal overlap, implying that the magnetic field in this region is rendered stochastic. The lower panel of Fig. 6 shows the predicted widths of the various magnetic island chains driven by the applied $n = 3$ RMP as functions of time, taking into account the shielding of driven magnetic reconnection by plasma flow. It is apparent that the shielded island widths are generally much smaller than the vacuum island widths.

However, the shielding breaks down at various resonant surfaces when the associated natural frequency is zero (see the lower panel of Fig. 5). In this situation, the driven island width is similar to the vacuum island width. Note that Fig. 6 is similar in conception to Fig. 23 of Ref. 58.

Figure 7 shows the widths of the regions of density and electron temperature flattening associated with the $n = 3$ magnetic island chains driven by the RMP in the pedestal region as functions of $\overline{q_{95}}$ and time. (See Sect. III.F in Ref. 23, as well as Refs. 59 and 60.) (Note that the energy diffusivity data shown in Fig. 3 is used to calculate the critical island width for electron temperature flattening, whereas the corresponding particle diffusivity data is used to calculate the critical island width for density flattening.⁵⁹ This distinction was not made in Ref. 23, which just used a generic perpendicular diffusivity for momentum, energy, and particles.) It can be seen that the driven magnetic island chains that do not lock to the RMP are generally too narrow to significantly flatten the density and electron temperature profiles, implying that there is actually very little degradation of the pedestal energy and particle confinement due to the applied RMP from such island chains. However, in those situations in which the shielding of driven magnetic reconnection due to plasma flow breaks down at a given resonant surface (i.e., the true natural frequency becomes zero), a locked magnetic island chain is generated that is wide enough to flatten both the density and the electron temperature profiles.

Ideally, in order to account for the ELM-suppression/mitigation windows in DIII-D discharge #145380, according to the standard hypothesis of how RMP-induced ELM-suppression operates, we require the major regions of density and temperature flattening to correspond to the intersections of the yellow vertical bands and the horizontal dotted lines in Fig. 7. If this is the case then the density and temperature profiles are locally flattened at the top of the pedestal (which corresponds to the horizontal dotted lines) during the ELM-suppression/mitigation windows (which correspond to the yellow vertical bands). (Note that the top of the pedestal is, somewhat arbitrarily, identified with the off-axis peak in the electron number density that is apparent in the top panel of Fig. 3.) It can be seen that the region of density and temperature flattening associated with the $m = 11$ (brown) tearing mode driven by the RMP lines up fairly well with the first ELM-suppression/mitigation window. The region of density and temperature flattening associated with the $m = 10$ (magenta) tearing mode lines up somewhat less well with the second ELM-

suppression/mitigation window. To be more exact, the region is located at the top of the pedestal, but occurs slightly too early. However, the region of density and temperature flattening associated with the $m = 9$ (cyan) tearing mode lines up very poorly with the third ELM-suppression/mitigation window. To be more exact, the region is not really located at the top of the pedestal, and occurs significantly too early. The ultimate reason for this poor alignment is that the major zero-crossing of the $m = 9$ natural frequency in the upper panel of Fig. 5 does not take place within the third ELM-suppression/mitigation window (unlike the major zero-crossings of the $m = 11$ and $m = 10$ natural frequencies, which do take place within the first and the second ELM-suppression/mitigation windows, respectively).

D. Case 2: $\varpi = \varpi_{\perp EB}$

The second case that we shall consider is that in which the natural frequency is determined by the local $\mathbf{E} \times \mathbf{B}$ velocity; in other words, the natural frequency is specified by Eq. (6).

Figures 8–10 show analogous data to Figs. 5–7, respectively. It can be seen from the upper panel of Fig. 8 that, in the absence of the RMP, the natural frequency of the $m = 11$ (brown), the $m = 10$ (magenta), and the $m = 9$ (cyan), tearing modes have their zero-crossings in the first, second, and third, ELM-suppression/mitigation window, respectively. As before, it is clear from the lower panel of Fig. 8 that these tearing modes lock to the RMP when the magnitudes of their unperturbed natural frequencies fall below about 5 krad/s. Likewise, it is apparent from Fig. 9 that the shielded island widths driven in the pedestal by the applied RMP are much smaller than the corresponding vacuum island widths, except when the islands lock to the RMP. Furthermore, according to Fig. 10, the regions of density and temperature flattening associated with the $m = 11$ (brown), the $m = 10$ (magenta), and the $m = 9$ (cyan), tearing modes driven by the RMP line up very well with the first, second, and third, ELM-suppression/mitigation windows, respectively. To be more exact, the regions are located at the top of the pedestal, and also occur in approximately the correct time intervals. Note that overlapping island chains are also driven at the bottom of the pedestal. We associate these chains with the density pump-out phenomenon.^{19,23} The chains at the bottom of the pedestal are more apparent in this particular case than in the other two cases considered in this paper because the diamagnetic contributions to the natural frequencies at the bottom of the pedestal (which are absent in the present case) are

comparatively large.

E. Case 3: $\varpi = \varpi_{\perp e}$

The final case that we shall consider is that in which the natural frequency is determined by the local electron fluid; in other words, the natural frequency is specified by Eq. (7).

Figures 11–13 show analogous data to Figs. 5–7 and Figs. 8–10, respectively. It can be seen from Fig 13 that there is no ELM suppression/mitigation window associated with the $m = 11$ mode. However, the ELM suppression/mitigation windows associated with the $m = 10$ and $m = 9$ modes occur in approximately the correct time intervals.

IV. SUMMARY AND DISCUSSION

The toroidal asymptotic matching model of the response of a tokamak plasma to a static RMP that is described in Ref. 23 has been implemented in the newly developed **EPEC** code (Extended Perturbed Equilibrium Code). The **EPEC** code has been used to simulate the three $n = 3$ RMP-induced ELM-suppression/mitigation windows in q_{95} that are evident when the plasma current is slowly ramped in DIII-D discharge #145380. All quantities employed in the simulation are derived from measurements taken in DIII-D discharge #145380, apart from the neutral particle data (which is taken from a much earlier discharge).

Three cases are considered. These cases are summarized in Fig. 14. (In this figure, the ELM/mitigation suppression windows are defined as the intersection of the regions of density flattening and the top of the pedestal in Figs. 7, 10, and 13.) In the first case, the natural frequencies of (stable) $n = 3$ tearing modes, resonant in the plasma, are assumed to be determined by the ion flows at the corresponding resonant surfaces, which is the prediction of nonlinear tearing mode theory.^{28,30,31} In the second case, the natural frequencies of (stable) $n = 3$ tearing modes, resonant in the plasma, are assumed to be determined by the $\mathbf{E} \times \mathbf{B}$ velocities at the corresponding resonant surfaces.^{15,32} In the third case, the natural frequencies of (stable) $n = 3$ tearing modes, resonant in the plasma, are assumed to be determined by the electron flows at the corresponding resonant surfaces, which is the prediction of linear tearing mode theory.^{35–37}

The first case only leads to partial agreement between the **EPEC** simulations and the

observations; in that, the first ELM suppression/mitigation window is missing. This lack of complete agreement is somewhat disappointing, given that the response of a tokamak plasma to an RMP ought to be correctly described by nonlinear tearing mode theory. However, according to nonlinear theory, the natural frequency of a tearing mode resonant close to the edge of a tokamak plasma is strongly affected by charge-exchange with neutrals.²³ In particular, the frequency depends on the poloidal asymmetry of the neutrals. To be more exact, if the neutrals are concentrated close to the X-point then the natural frequency is pulled in the electron diamagnetic direction, and vice versa.²³ (See Sect. IV of Ref. 23.) Thus, given our comparative ignorance of the neutral particle distribution in DIII-D discharge #145380, it would be premature to write-off the nonlinear prediction at this stage.

The second case gives the best agreement between the EPEC simulations and the observations. To be more exact, the second case leads to the prediction that comparatively wide locked magnetic island chains, that locally flatten the density and temperature profiles, are present at the top of the pedestal during the ELM-suppression/mitigation windows, and are absent otherwise. This prediction is in accordance with the prevailing hypothesis that ELM suppression is due to the appearance of locked magnetic island chains at the top of the pedestal that locally flatten the pressure profile, thereby preventing the pedestal width from growing radially and achieving a large enough value to trigger peeling-ballooning modes.²¹

The third case only leads to partial agreement between the EPEC simulations and the observations; in that, the third ELM suppression/mitigation window is missing. This lack of agreement is probably due to that fact that the response of a tokamak plasma to an RMP is not accurately described by linear tearing mode theory.²²

ACKNOWLEDGEMENTS

The author would like to thank Q.M. Hu and R. Nazikian for providing the experimental data used in this paper. The author would also like to thank J.-K. Park and N.C. Logan for providing guidance on how to run the GPEC code. Finally, the author would like to thank C. Paz-Solden, B.A. Grierson, and W.M. Solomon for helpful comments during the preparation of this paper.

This research was directly funded by the U.S. Department of Energy, Office of Science, Office of Fusion Energy Sciences, under contract DE-FG02-04ER54742, and incorporates

work funded by the U.S. Department of Energy, Office of Science, Office of Fusion Energy Sciences, using the DIII-D National Fusion Facility, a DOE Office of Science user facility, under contract DE-FC02-04ER54698.

DISCLAIMER

This report was prepared as an account of work sponsored by an agency of the United States Government. Neither the United States Government nor any agency thereof, nor any of their employees, makes any warranty, express or implied, or assumes any legal liability or responsibility for the accuracy, completeness, or usefulness of any information, apparatus, product, or process disclosed, or represents that its use would not infringe privately owned rights. Reference herein to any specific commercial product, process, or service by trade name, trademark, manufacturer, or otherwise does not necessarily constitute or imply its endorsement, recommendation, or favoring by the United States Government or any agency thereof. The views and opinions of authors expressed herein do not necessarily state or reflect those of the United States Government or any agency thereof.

DATA AVAILABILITY STATEMENT

The data that support the findings of this study are available from the corresponding author upon reasonable request.

REFERENCES

-
- ¹ F. Wagner, G. Becker, K. Behringer, D. Campbell, A. Eberhagen, W. Engelhardt, G. Fussmann, O. Gehre, J. Gernhardt, G. v. Gierke, *et al.*, Phys. Rev. Lett. **49**, 1408 (1982).
 - ² H. Zohm, Plasma Phys. Control. Fusion **38**, 105 (1996).
 - ³ A. Loarte, G. Saibene, R. Sartori, M. Bécoulet, L. Horton, T. Eich, A. Herrmann, M. Laux, G. Matthews, S. Jachmich, *et al.*, J. Nucl. Materials **313–316**, 962 (2003).

- ⁴ T.E. Evans, R.A. Moyer, J.G. Watkins, P.R. Thomas, T.H. Osborne, J.A. Boedo, M.E. Fenstermacher, K.H. Finken, R.J. Groebner, M. Groth, *et al.*, Phys. Rev. Lett. **92**, 235003 (2004).
- ⁵ Y. Liang, H.R. Koslowski, P.R. Thomas, E. Nardon, B. Alper, P. Andrew, Y. Andrew, G. Arnoux, Y. Baranov, M. Bécoulet, *et al.*, Phys. Rev. Lett. **98**, 265004 (2007).
- ⁶ W. Suttrop, T. Eich, J.C. Fuchs, S. Günter, A. Janzer, A. Herrmann, A. Kallenbach, P.T. Lang, T. Lunt, M. Maraschek, *et al.*, Phys. Rev. Lett. **106**, 225004 (2011).
- ⁷ Y.M. Jeon, J.-K. Park, S.W. Yoon, W.H. Ko, S.G. Lee, K.D. Lee, G.S. Yun, Y.U. Nam, W.C. Kim, J.-G. Kwak, K.S. Lee, H.K. Kim, and H.L. Yang, *et al.*, Phys. Rev. Lett. **109**, 035004 (2012).
- ⁸ A. Kirk, I.T. Chapman, Y. Liu, P. Cahyna, P. Denner, G. Fishpool, C.J. Ham, J.R. Harrison, Y. Liang, E. Nardon, S. Saarelma, R. Scannell, A.J. Thornton, and MAST Team, Nucl. Fusion **53**, 043007 (2013).
- ⁹ T. Sun, Y. Liang, Y.Q. Liu, S. Gu, X. Yang, W. Guo, T. Shi, M. Jia, L. Wang, B. Lyu, *et al.*, Phys. Rev. Lett. **117**, 115001 (2016).
- ¹⁰ O. Schmitz, T.E. Evans, M.E. Fenstermacher, M. Lehnen, H. Stoschus, E.A. Unterberg, J.W. Coenen, H. Frerichs, M.W. Jakubowski, R. Laengner, *et al.*, Nucl. Fusion **52**, 043005 (2012).
- ¹¹ M.J. Lanctot, R.J. Buttery, J.S. de Grassie, T.E. Evans, N.M. Ferraro, J.M. Hanson, S.R. Haskey, R.A. Moyer, R. Nazikian, T.H. Osborne, *et al.*, Nucl. Fusion **53**, 083019 (2013).
- ¹² C. Paz-Solden, R. Nazikian, S.R. Haskey, N.C. Logan, E.J. Strait, N.M. Ferraro, J.M. Hanson, J.D. King, M.J. Lanctot, R.A. Moyer, *et al.*, Phys. Rev. Lett. **114**, 105001 (2015).
- ¹³ R. Nazikian, C. Paz-Soldan, J.D. Callen, J.S. de Grassie, D. Eldon, T.E. Evans, N.M. Ferraro, B.A. Grierson, R.J. Groebner, S.R. Haskey, *et al.*, Phys. Rev. Lett. **114**, 105002 (2015).
- ¹⁴ B.C. Lyons, N.M. Ferraro, C. Paz-Solden, R. Nazikian, and A. Wingen, Plasma Phys. Contol. Fusion **59**, 044001(2017).
- ¹⁵ C. Paz-Solden, R. Nazikian, L. Cui, B.C. Lyons, D.M. Orlov, A. Kirk, N.C. Logan, T.H. Osborne, W. Suttrop, and D.B. Weisberg, Nucl. Fusion **59**, 056012 (2019).
- ¹⁶ Q. Yu, S. Günter, and B.D. Scott, Phys. Plasmas **10**, 797 (2003).

- ¹⁷ Q. Yu, Nucl. Fusion **50**, 025014 (2010).
- ¹⁸ Q. Yu, and S. Günter, Nucl. Fusion **51**, 073030 (2011).
- ¹⁹ Q.M. Hu, R. Nazikian, B.A. Grierson, N.C. Logan, J.-K. Park, C. Paz-Soldan, and Q. Yu, Phys. Plasmas **26**, 120702 (2019).
- ²⁰ J.W. Connor, R.J. Hastie, H.R. Wilson, and R.L. Miller, Phys. Plasmas **5**, 2687 (1998).
- ²¹ P.B. Snyder, T.H. Osbourne, K.H. Burrell, R.J. Groebner, A.W. Leonard, R. Nazikian, D.M. Orlov, O. Schmitz, M.R. Wade, and H.R. Wilson, Phys. Plasmas **19**, 056115 (2012).
- ²² R. Fitzpatrick, Phys. Plasmas **27**, 042506 (2020).
- ²³ R. Fitzpatrick, and A.O. Nelson, Phys. Plasmas **27**, 072501 (2020).
- ²⁴ Q.M. Hu, R. Nazikian, B.A. Grierson, N.C. Logan, D.M. Orlov, C. Paz-Soldan, and Q. Yu, Phys. Rev. Lett. **125**, 045001 (2020).
- ²⁵ R. Fitzpatrick, Nucl. Fusion **33**, 1049 (1993).
- ²⁶ R. Fitzpatrick, Phys. Plasmas **5**, 3325 (1998).
- ²⁷ G. Ara, B. Basu, B. Coppi, G. Laval, M.N. Rosenbluth, and B.V. Waddell, Ann. Phys. (N.Y.) **112**, 443 (1978).
- ²⁸ R. Fitzpatrick, and F.L. Waelbroeck, Phys. Plasmas **12**, 022307 (2005).
- ²⁹ R. Fitzpatrick, P.G. Watson, and F.L. Waelbroeck, Phys. Plasmas **12**, 082510 (2005).
- ³⁰ R. Fitzpatrick, Phys. Plasmas **25**, 042503 (2018).
- ³¹ R. Fitzpatrick, Phys. Plasmas **25**, 112505 (2018).
- ³² M.F. Heyn, I.B. Ivanov, S.V. Kasilov, W. Kernbichler, I. Joseph, R.A. Moyer, and A.M. Runov, Nucl. Fusion **48**, 024005 (2008).
- ³³ R. Fitzpatrick, and T.C. Hender, Phys. Fluids B **3**, 644 (1991).
- ³⁴ A. Cole, and R. Fitzpatrick, Phys. Plasmas **13**, 032503 (2006).
- ³⁵ M. Bécoulet, F. Orain, P. Maget, N. Mellet, X. Garbet, E. Nardon, G.T.A. Huysmans, T. Caspar, A. Loarte, P. Cayna, *et al.*, Nucl. Fusion **52**, 054003 (2012).
- ³⁶ N.M. Ferraro, Phys. Plasmas **19**, 056105 (2012).
- ³⁷ F. Orain, M. Bécoulet, G. Dif-Pradalier, G.T.A. Huysmans, S. Pamela, E. Nardon, C. Passeron, G. Latu, V. Grandgirard, A. Fil, *et al.*, Phys. Plasmas **20**, 102510 (2013).

- ³⁸ H.P. Furth, J. Killeen, and M.N. Rosenbluth, Phys. Fluids **6**, 459 (1963).
- ³⁹ B. Coppi, J.M. Greene, and J.L. Johnson, Nucl. Fusion **6**, 101 (1966).
- ⁴⁰ P.H. Rutherford, Phys. Fluids **16**, 1903 (1973).
- ⁴¹ A. Pletzer, and R.L. Dewar, J. Plasma Physics **45**, 427 (1991).
- ⁴² R. Fitzpatrick, R.J. Hastie, T.J. Martin, and C.M. Roach, Nucl. Fusion **33**, 1533 (1993).
- ⁴³ A. Pletzer, A. Bondeson, and R.L. Dewar, J. Comp. Phys. **115**, 530 (1994).
- ⁴⁴ S. Tokuda, Nucl. Fusion **41**, 1037 (2001).
- ⁴⁵ D.P. Brennan, R.J. La Haye, A.D. Turnbull, M.S. Chu, T.H. Jensen, L.L. Lao, T.C. Luce, P.A. Politzer, and E.J. Strait, Phys. Plasmas **10**, 1643 (2003).
- ⁴⁶ M. Furukawa, and S. Tokuda, Phys. Plasmas **19**, 102511 (2012).
- ⁴⁷ A.H. Glasser, Z.R. Wang, and J.-K. Park, Phys. Plasmas **23**, 112506 (2016).
- ⁴⁸ R. Fitzpatrick, Phys. Plasmas **24**, 072506 (2017).
- ⁴⁹ S.R. Haskey, M.J. Lanctot, Y.Q. Liu, C. Paz-Soldan, J.D. King, B.D. Blackwell, and O. Schmitz, Plasma Phys. Control. Fusion **57**, 025015 (2015).
- ⁵⁰ D.A. Ryan, Y.Q. Liu, A. Kirk, W. Suttrop, B. Dudson, M. Dunne, R. Fischer, J.C. Fuchs, M. Garcia-Munoz, B. Kurzan, *et al.*, Plasma Phys. Control. Fusion **57**, 095008 (2015).
- ⁵¹ J. K. Park, M.J. Schaffer, J.E. Menard, and A.H. Boozer, Phys. Rev. Lett. **99**, 195003 (2007).
- ⁵² J.K. Park, and N.C. Logan, Phys. Plasmas **24**, 032505 (2017).
- ⁵³ G.L. Jackson, P.M. Anderson, J. Bialek, W.P. Cary, G.L. Campbell, A.M. Garofalo, R. Hatcher, A.G. Kellman, R.J. La Haye, A. Nagy, *et al.*, Proc. 30th EPS Conf. on Controlled Fusion and Plasma Physics. (St. Petersburg, Russia, 2003) CD-ROM, P-4.47.
- ⁵⁴ R.J. Hawryluk, *Physics of Plasma Close to Thermonuclear Conditions: Vol. 1.* (Commission of the European Communities, Brussels, 1980.) Internal Document DUR-FU-BRU-XII/476180.
- ⁵⁵ P. Monier-Garbet, K.H. Burrell, F.L. Hinton, J. Kim, X. Garbet, and R.J. Groebner, Nucl. Fusion **37**, 403 (1997).
- ⁵⁶ A. Rosenthal, and F.M. Laggner, private communication (2020).
- ⁵⁷ S. Wiesen, D. Reiter, V. Kotov, M. Baelmans, W. Dekeyser, A.S. Kukushkin, S.W. Lisgo, R.A. Pitts, V. Rozhansky, G. Saibene I. Veselova, and S. Voskoboynikov, J. Nucl. Mat. **468**,

480 (2015).

- ⁵⁸ M.R. Wade, R. Nazikian, J.D. de Grassie, T.E. Evans, N.M. Ferraro, R.A. Moyer, D.M. Orlov, R.J. Buttery, M.E. Fenstermacher, A.M. Garofalo, *et al.*, Nucl. Fusion **55**, 023002 (2015).
- ⁵⁹ R. Fitzpatrick, Phys. Plasmas **2**, 825 (1995).
- ⁶⁰ N.N. Gorelenkov, R.V. Budny, Z. Chang, M.V. Gorelenkova, and L.E. Zakharov, Phys. Plasmas **3**, 3379 (1996).

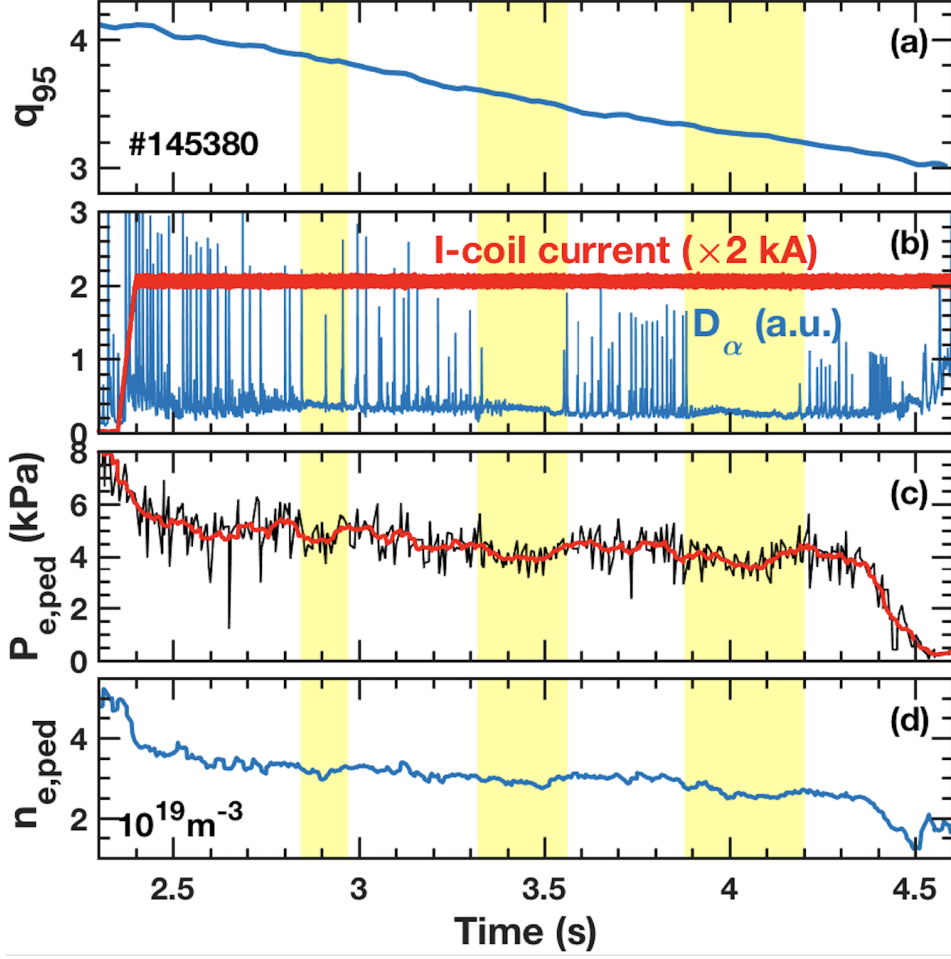


FIG. 1. Overview of DIII-D discharge #145380. (a) Safety factor at $\Psi_N = 0.95$. (b) D_α (i.e., Deuterium Balmer-alpha) signal, as well as $n = 3$ current flowing in upper and lower sections of I-coil. (c) Pedestal (i.e., $\Psi_N = 0.94$) electron pressure. (The red curve is the running average over 10 ms.) (d) Pedestal electron number density. The common vertical yellow bands indicate the ELM-suppression/mitigation windows.

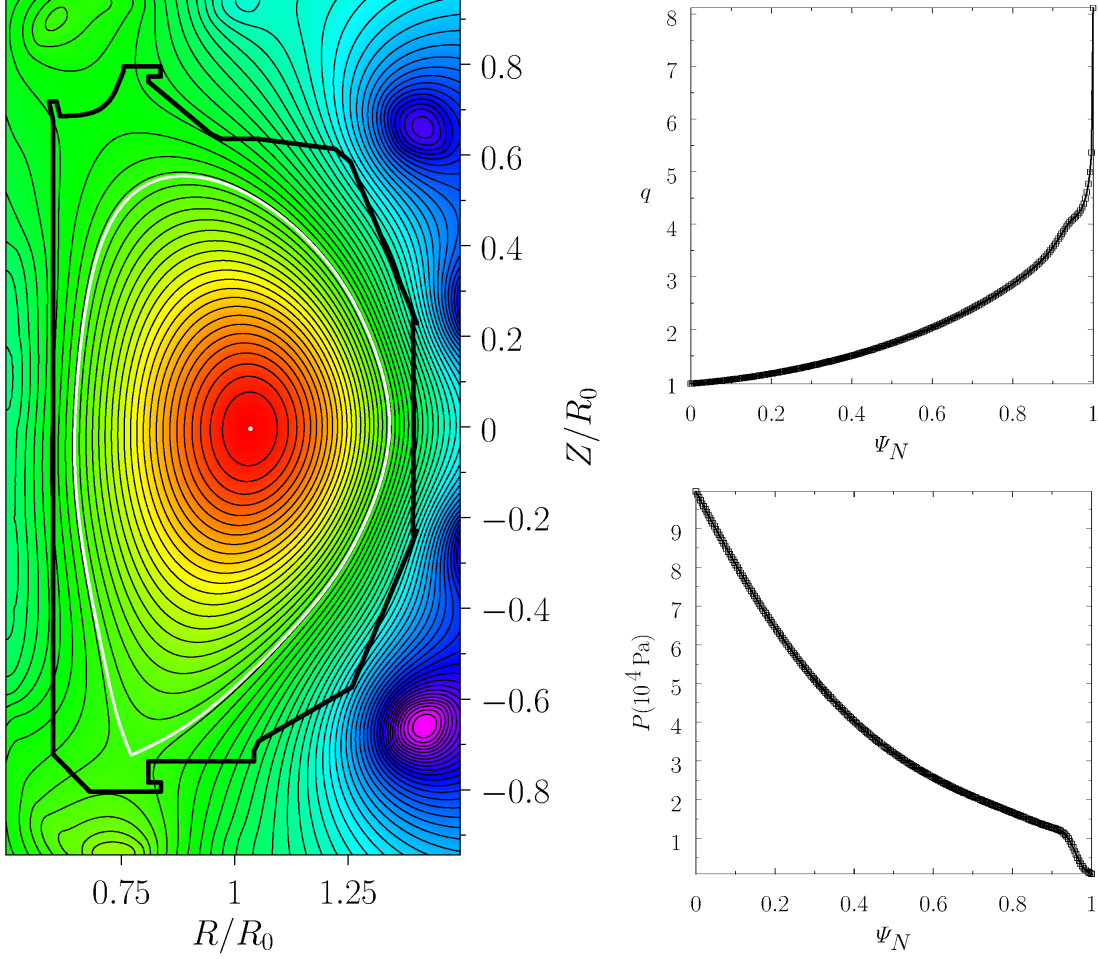


FIG. 2. Left Panel: Contours of the equilibrium poloidal magnetic flux in DIII-D discharge #145380 at time $t = 2500$ ms. The scale major radius is $R_0 = 1.70$ m. The white dot indicates the magnetic axis, the white curve indicates the last closed magnetic flux-surface, and the thick black line indicates the limiter. Upper-Right Panel: Safety-factor profile in DIII-D discharge #145380 at time $t = 2500$ ms. Lower-Right Panel: Total plasma pressure profile in DIII-D discharge #145380 at time $t = 2500$ ms.

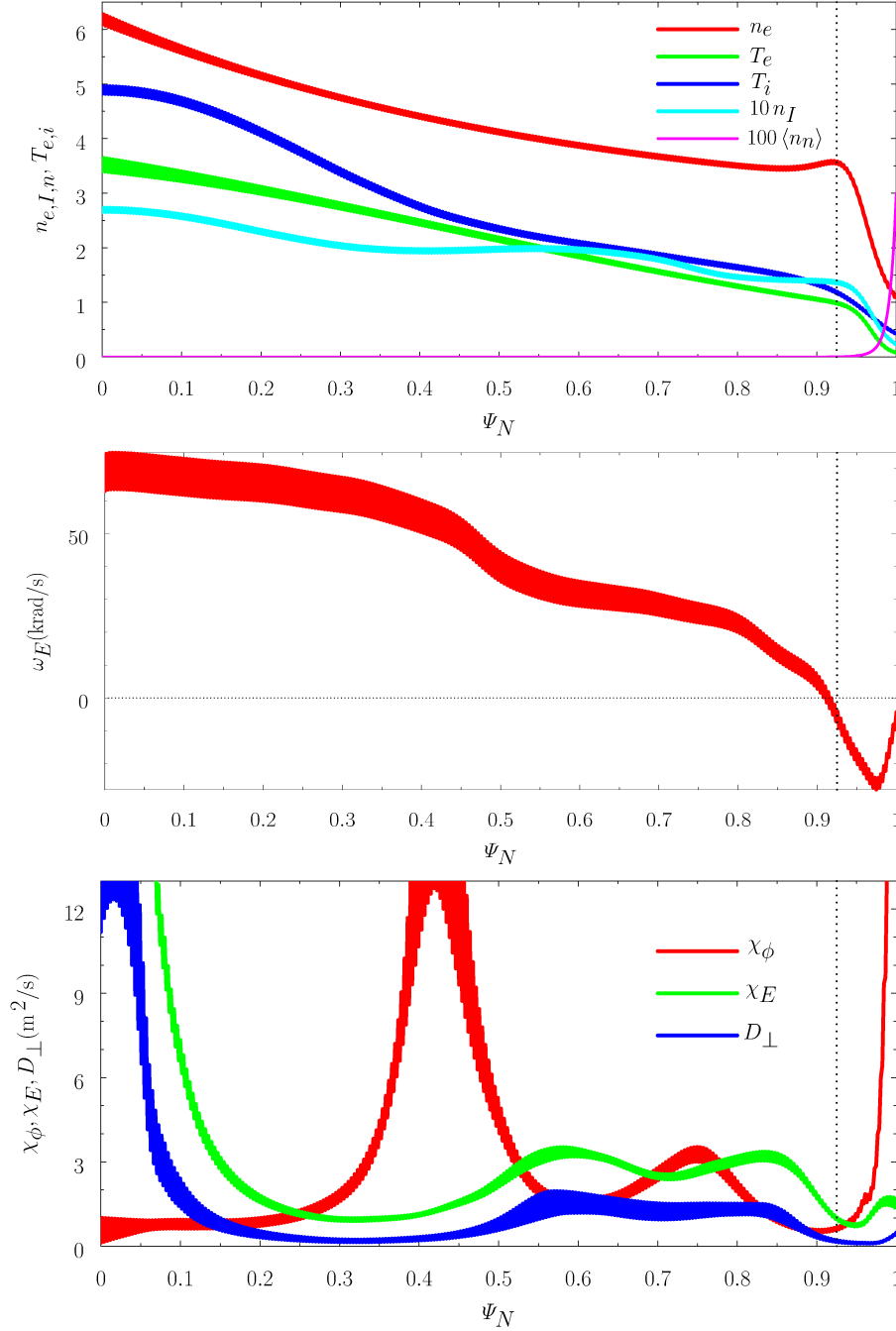


FIG. 3. Top Panel: The red, green, blue, cyan, and magenta curves show the electron number density (10^{19} m^{-3}), electron temperature (keV), (thermal) ion temperature (keV), C-VI ion number density (10^{18} m^{-3}), and flux-surface averaged neutral density (10^{17} m^{-3}) profiles, respectively, in DIII-D discharge #145380 at time $t = 2500$ ms. Middle Panel: $\mathbf{E} \times \mathbf{B}$ frequency profile in DIII-D discharge #145380 at time $t = 2500$. Bottom Panel: The red, green, and blue curves show the perpendicular momentum (χ_ϕ), energy (χ_E), and particle (D_\perp) diffusivity profiles, respectively, in DIII-D discharge #145380 at time $t = 2500$ ms. The common vertical dotted lines indicate the location of the top of the pedestal, $\psi_N = 0.925$. In all cases, the thickness of the curves indicate the uncertainties in the measurements.

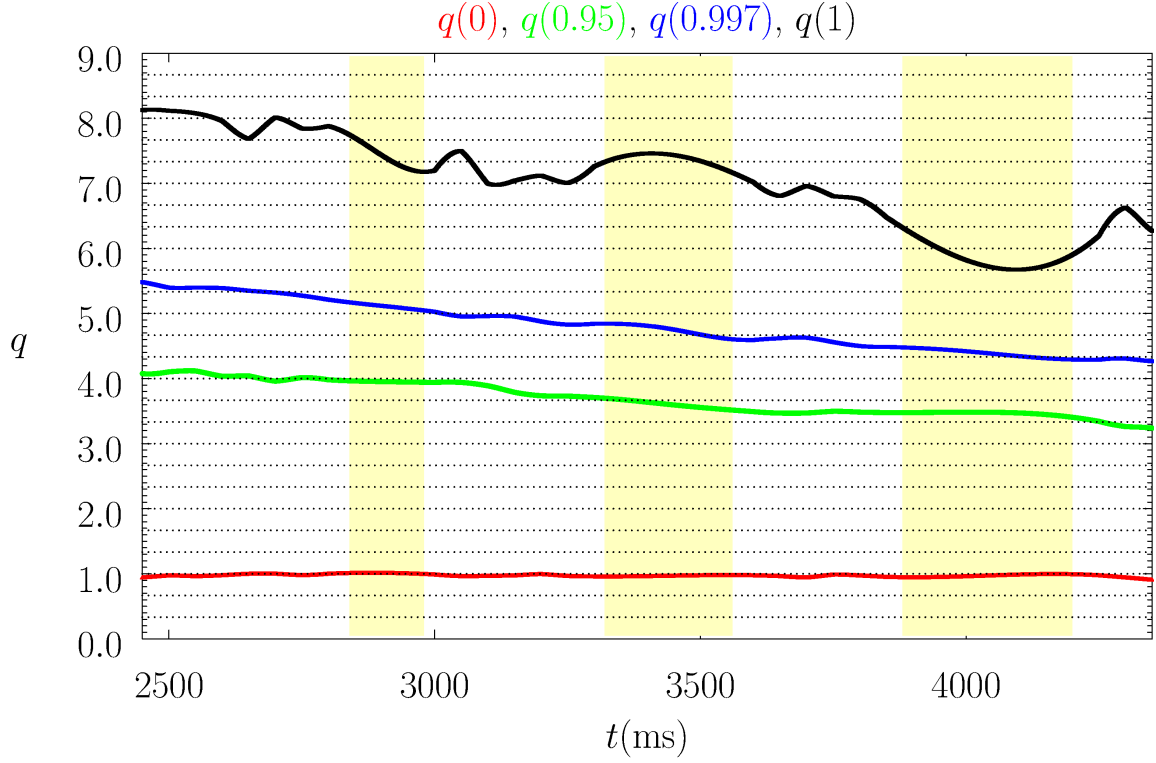


FIG. 4. Safety-factors as functions of time in DIII-D discharge #145380. The red, green, blue, and black curves show the safety-factors at the magnetic axis ($\Psi_N = 0.00$), the 95% flux surface ($\Psi_N = 0.950$), the effective plasma boundary for the GPEC and EPEC calculations ($\Psi_N = 0.997$), and the true plasma boundary ($\Psi_N = 1.00$), respectively. The yellow vertical bands indicate the ELM-suppression/mitigation windows. The horizontal dotted lines indicate the safety-factors at the various $n = 3$ rational surfaces.

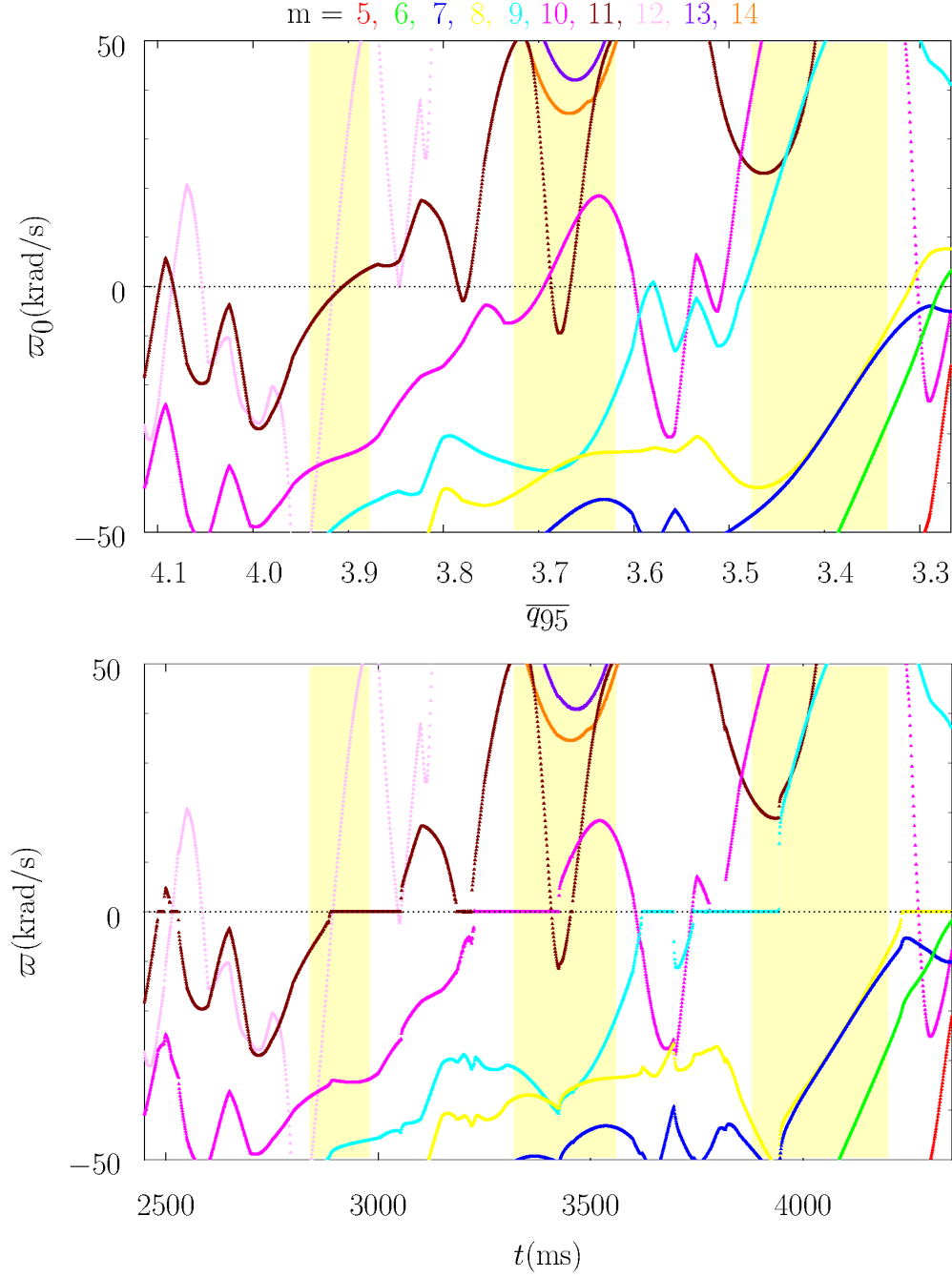


FIG. 5. Top Panel: $n = 3$ natural frequencies, in absence of RMP, as functions of the least-squares linear fit to q_{95} versus time in DIII-D discharge #145380, assuming that the natural frequency is determined by nonlinear island physics. Bottom Panel: $n = 3$ natural frequencies, in presence of RMP, as functions of time in DIII-D discharge #145380, assuming that the natural frequency is determined by nonlinear island physics. The red, green, blue, yellow, cyan, magenta, brown, pink, purple, and orange curves correspond to $m = 5, 6, 7, 8, 9, 10, 11, 12, 13$, and 14 , respectively. The yellow vertical bands indicate the ELM-suppression windows.

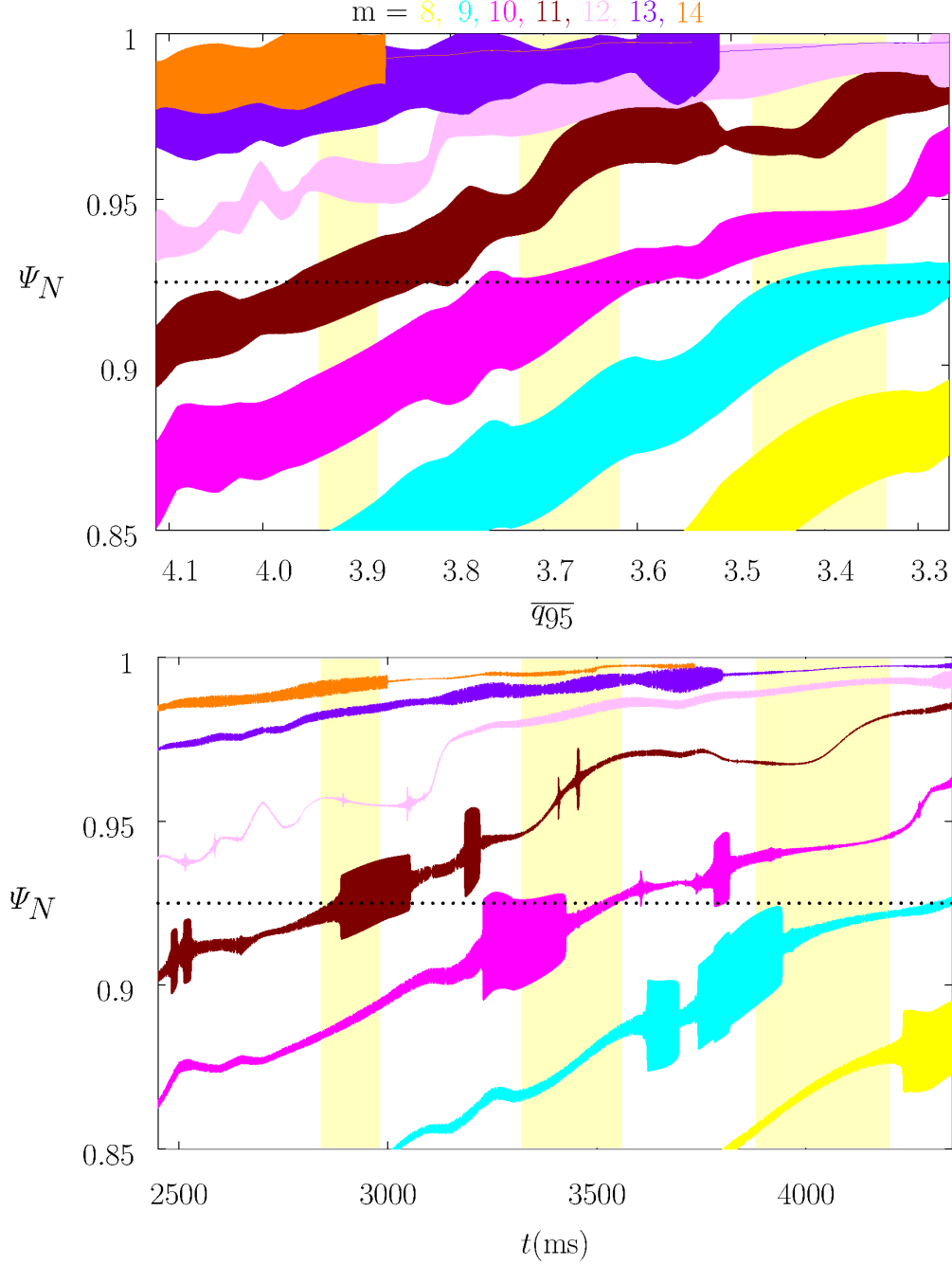


FIG. 6. Top Panel: Full $n = 3$ vacuum island widths as functions of the least-squares linear fit to q_{95} versus time in DIII-D discharge #145380. Bottom Panel: Full $n = 3$ island widths as functions of time in DIII-D discharge #145380, assuming that the natural frequency is determined by nonlinear island physics. The yellow, cyan, magenta, brown, pink, purple, and orange areas correspond to $m = 8, 9, 10, 11, 12, 13$, and 14 , respectively. The yellow vertical bands indicate the ELM-suppression/mitigation windows. The horizontal dotted lines indicate the top of the pedestal, $\Psi_N = 0.925$.

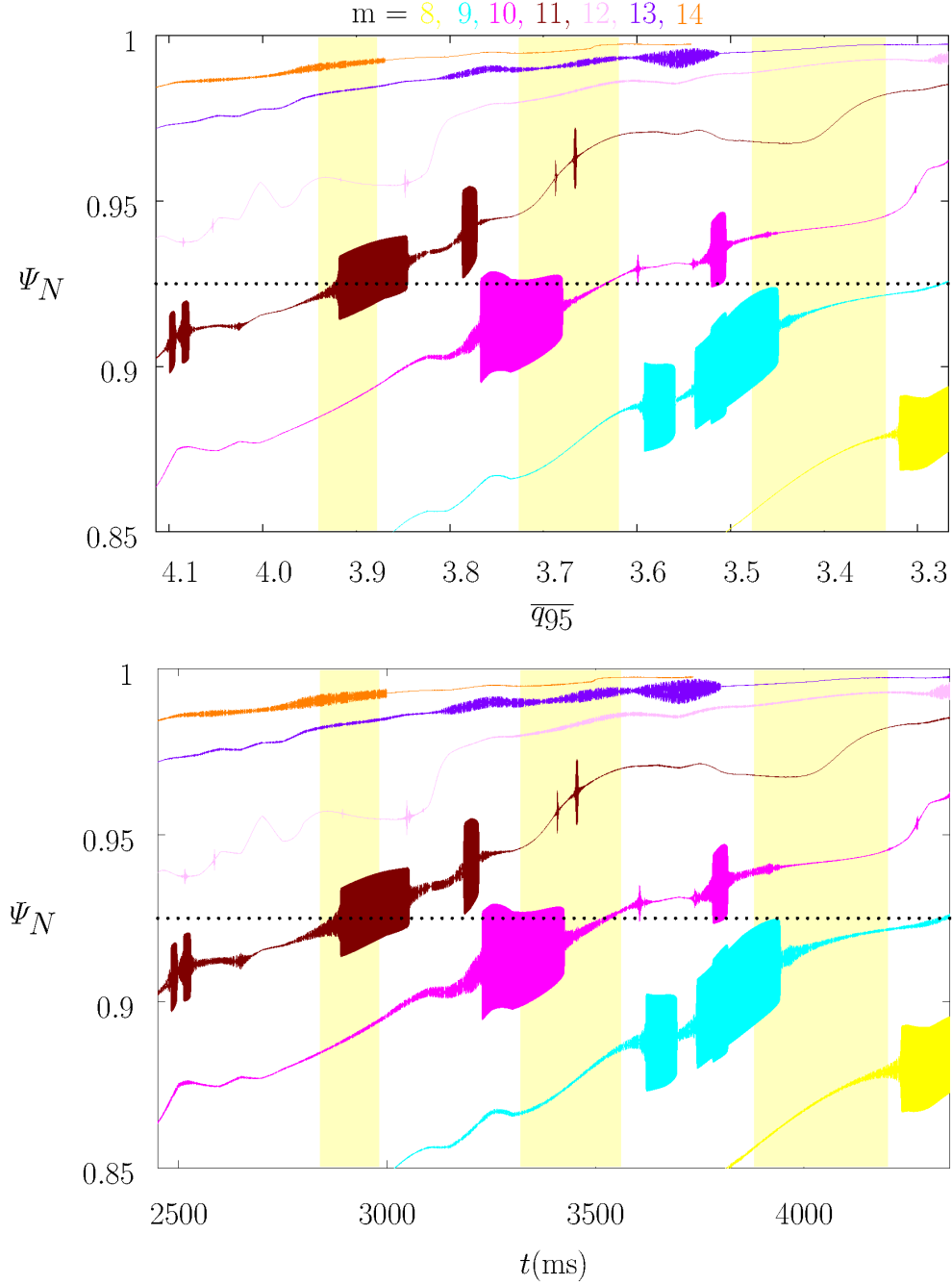


FIG. 7. Top Panel: Density flattening widths associated with induced $n = 3$ magnetic island chains as functions of the least-squares linear fit to q_{95} versus time in DIII-D discharge #145380, assuming that the natural frequency is determined by nonlinear island physics. Bottom Panel: Electron temperature flattening widths associated with induced $n = 3$ magnetic island chains as functions of time in DIII-D discharge #145380, assuming that the natural frequency is determined by nonlinear island physics. The yellow, cyan, magenta, brown, pink, purple, and orange areas correspond to $m = 8, 9, 10, 11, 12, 13$, and 14 , respectively. The yellow vertical bands indicate the ELM-suppression/mitigation windows. The horizontal dotted lines indicate the top of the pedestal, $\Psi_N = 0.925$.

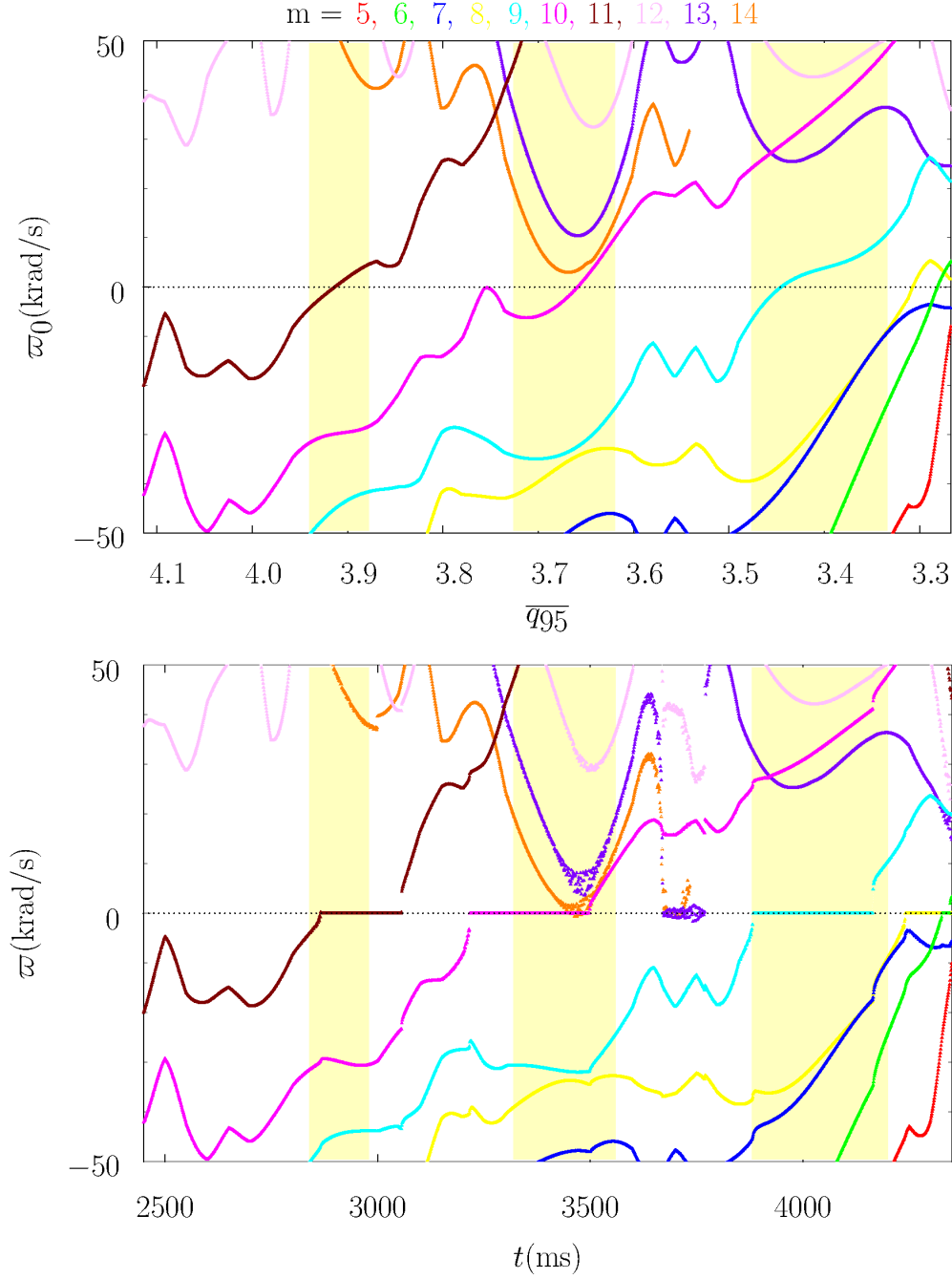


FIG. 8. Top Panel: $n = 3$ natural frequencies, in absence of RMP, as functions of the least-squares linear fit to q_{95} versus time in DIII-D discharge #145380, assuming that the natural frequency is determined by the local $\mathbf{E} \times \mathbf{B}$ velocity. Bottom Panel: $n = 3$ natural frequencies, in presence of RMP, as functions of time in DIII-D discharge #145380, assuming that the natural frequency is determined by the local $\mathbf{E} \times \mathbf{B}$ velocity. The red, green, blue, yellow, cyan, magenta, brown, pink, purple, and orange curves correspond to $m = 5, 6, 7, 8, 9, 10, 11, 12, 13$, and 14 , respectively. The yellow vertical bands indicate the ELM-suppression/mitigation windows.

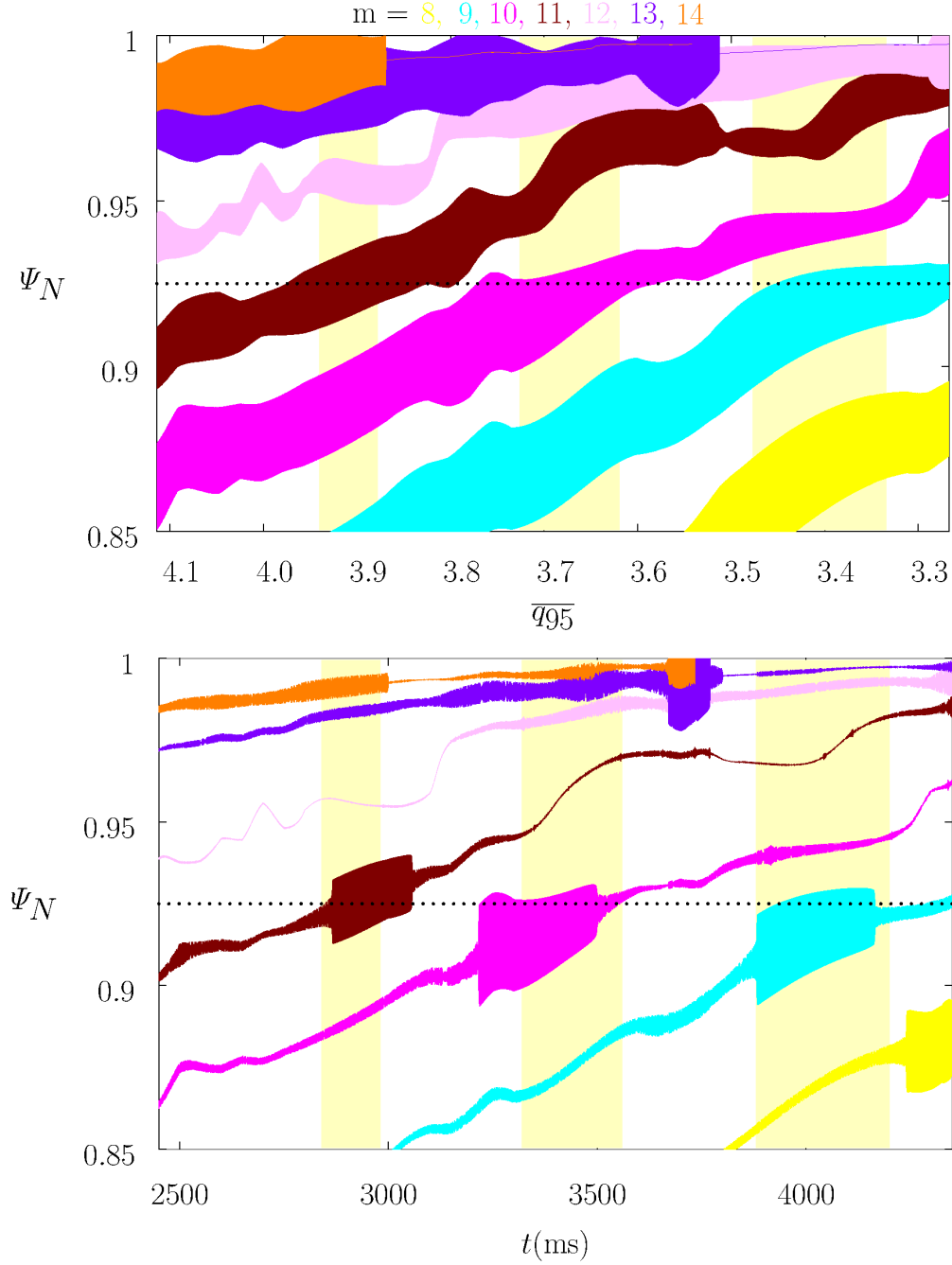


FIG. 9. Top Panel: $n = 3$ vacuum island widths as functions of the least-squares linear fit to q_{95} versus time in DIII-D discharge #145380. Bottom Panel: $n = 3$ island widths as functions of time in DIII-D discharge #145380, assuming that the natural frequency is determined by the local $\mathbf{E} \times \mathbf{B}$ velocity. The yellow, cyan, magenta, brown, pink, purple, and orange areas correspond to $m = 8, 9, 10, 11, 12, 13$, and 14 , respectively. The yellow vertical bands indicate the ELM-suppression/mitigation windows. The horizontal dotted lines indicate the top of the pedestal, $\Psi_N = 0.925$.

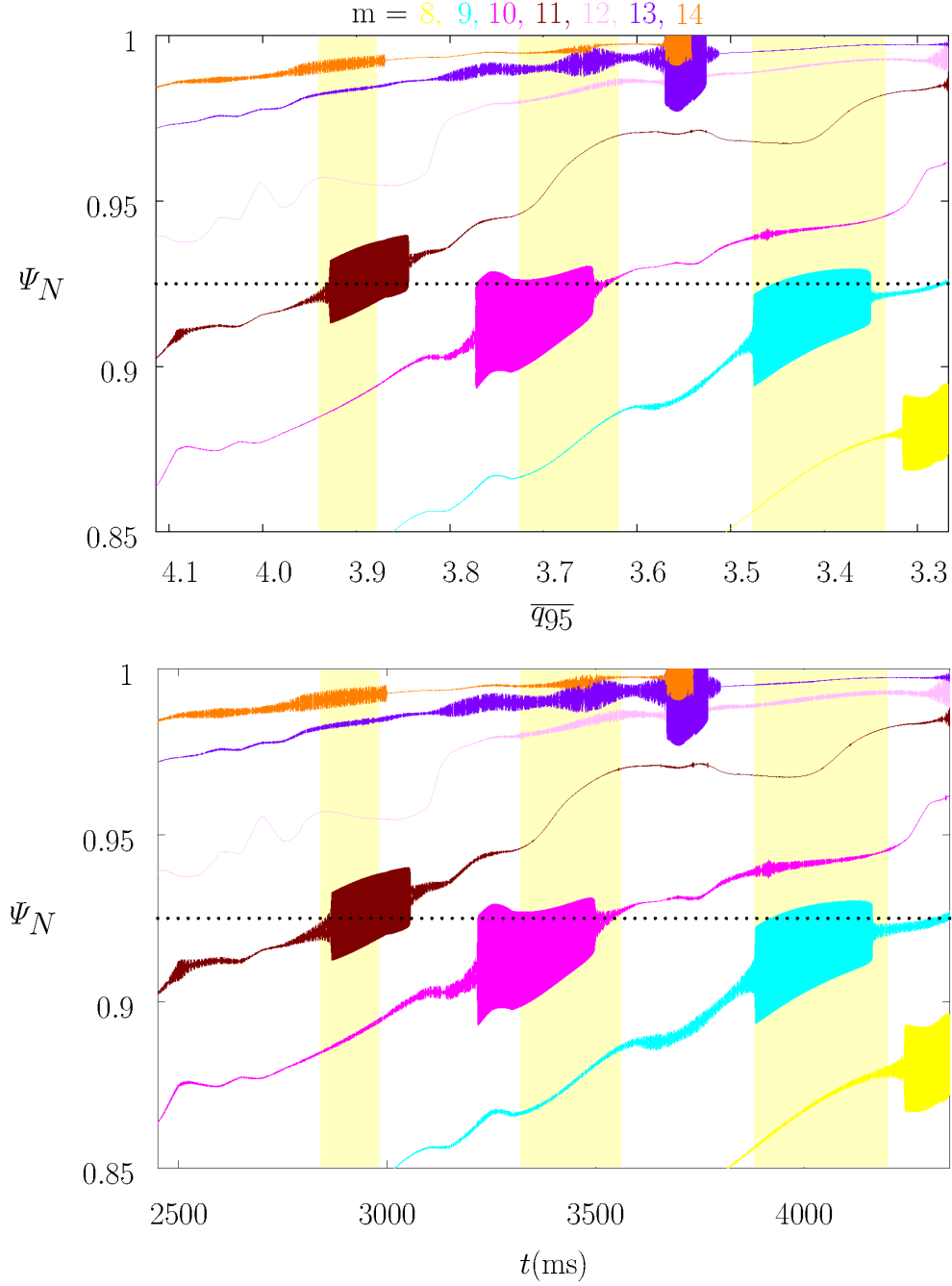


FIG. 10. Top Panel: Density flattening widths associated with induced $n = 3$ magnetic island chains as functions of the least-squares linear fit to q_{95} versus time in DIII-D discharge #145380, assuming that the natural frequency is determined by the local $\mathbf{E} \times \mathbf{B}$ velocity. Bottom Panel: Electron temperature flattening widths associated with induced $n = 3$ magnetic island chains as functions of time in DIII-D discharge #145380, assuming that the natural frequency is determined by the local $\mathbf{E} \times \mathbf{B}$ velocity. The yellow, cyan, magenta, brown, pink, purple, and orange areas correspond to $m = 8, 9, 10, 11, 12, 13$, and 14 , respectively. The yellow vertical bands indicate the ELM-suppression/mitigation windows. The horizontal dotted lines indicate the top of the pedestal, $\Psi_N = 0.925$.

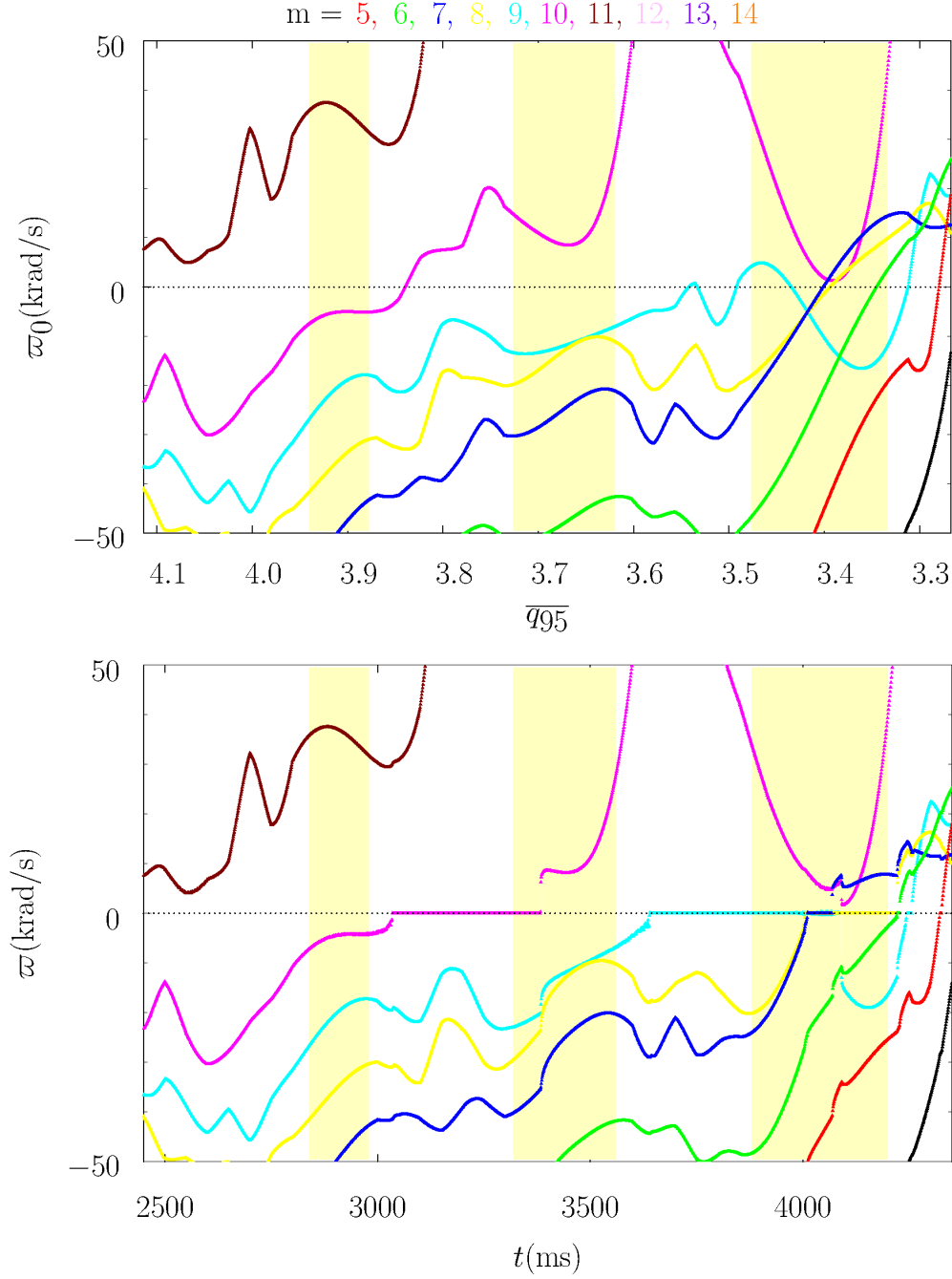


FIG. 11. Top Panel: $n = 3$ natural frequencies, in absence of RMP, as functions of the least-squares linear fit to q_{95} versus time in DIII-D discharge #145380, assuming that the natural frequency is determined by linear layer physics. Bottom Panel: $n = 3$ natural frequencies, in presence of RMP, as functions of time in DIII-D discharge #145380, assuming that the natural frequency is determined by linear layer physics. The black, red, green, blue, yellow, cyan, magenta, brown, purple, and orange curves correspond to $m = 4, 5, 6, 7, 8, 9, 10, 11, 13$, and 14, respectively. The yellow vertical bands indicate the ELM-suppression/mitigation windows.

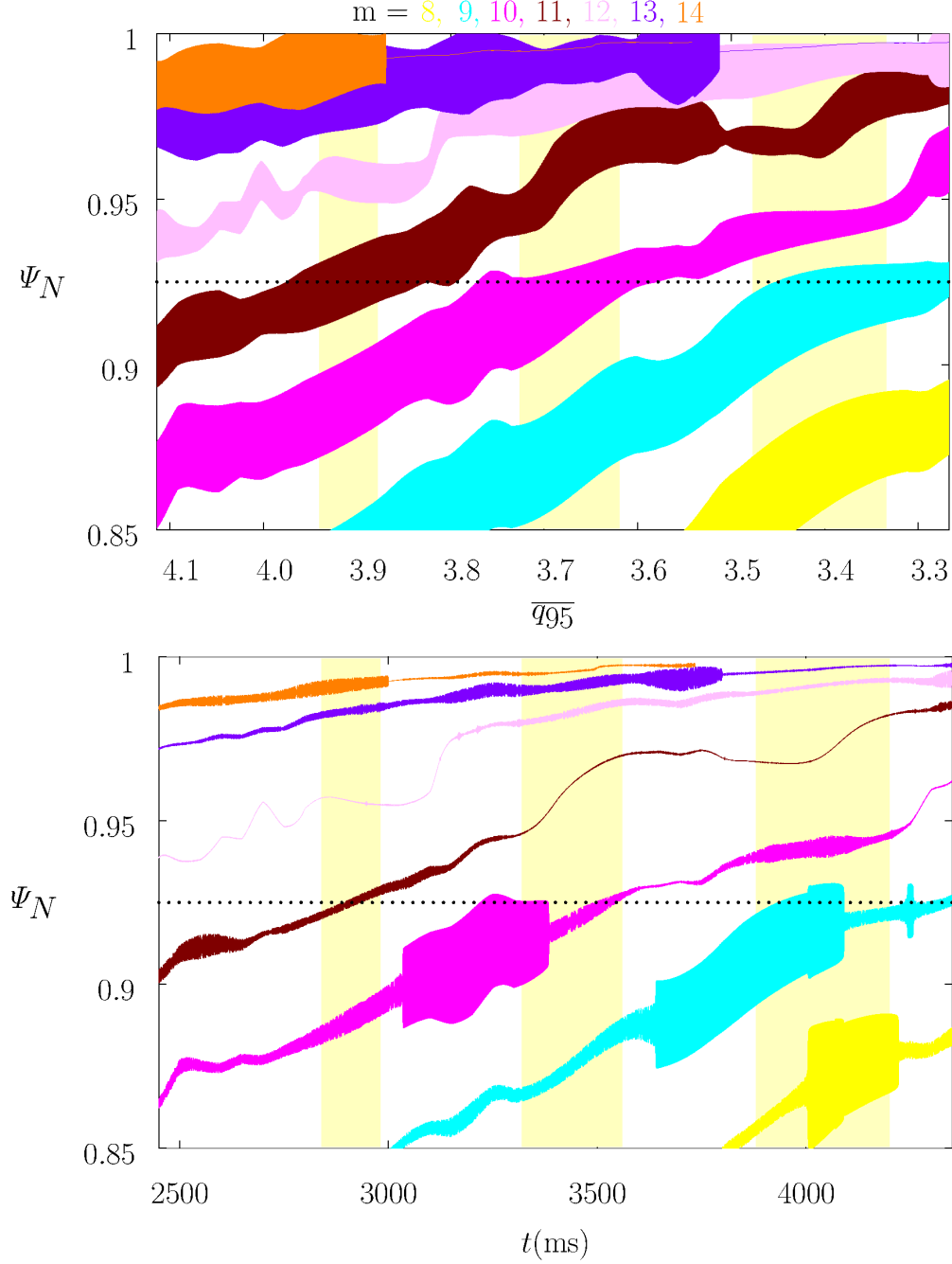


FIG. 12. Top Panel: $n = 3$ vacuum island widths as functions of the least-squares linear fit to q_{95} versus time in DIII-D discharge #145380. Bottom Panel: $n = 3$ island widths as functions of time in DIII-D discharge #145380, assuming that the natural frequency is determined by linear layer physics. The yellow, cyan, magenta, brown, pink, purple, and orange areas correspond to $m = 8, 9, 10, 11, 12, 13$, and 14 , respectively. The yellow vertical bands indicate the ELM-suppression/mitigation windows. The horizontal dotted lines indicate the top of the pedestal, $\Psi_N = 0.925$.

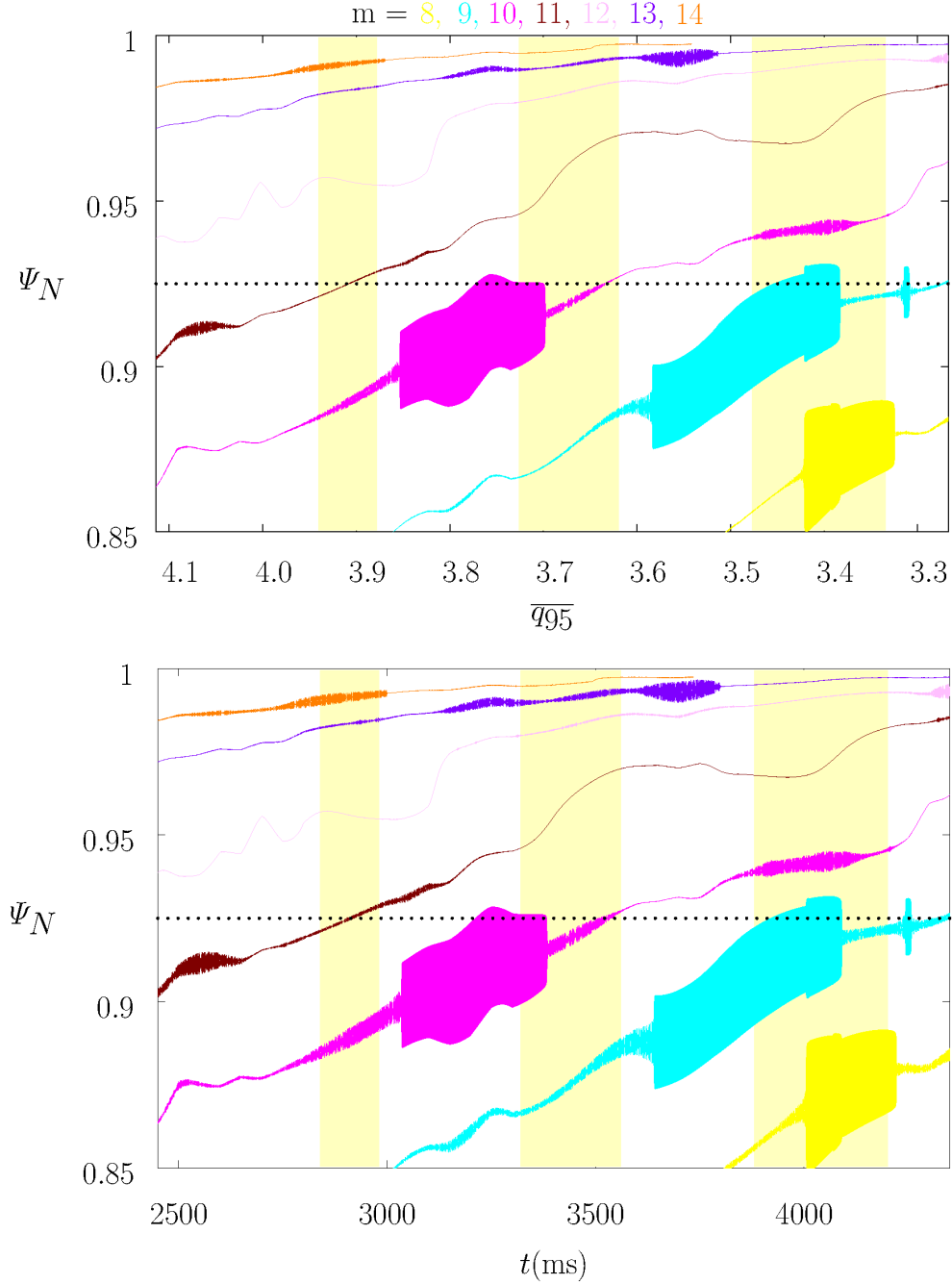


FIG. 13. Top Panel: Density flattening widths associated with induced $n = 3$ magnetic island chains as functions of the least-squares linear fit to q_{95} versus time in DIII-D discharge #145380, assuming that the natural frequency is determined by linear layer physics. Bottom Panel: Electron temperature flattening widths associated with induced $n = 3$ magnetic island chains as functions of time in DIII-D discharge #145380, assuming that the natural frequency is determined by linear layer physics. The yellow, cyan, magenta, brown, pink, purple, and orange areas correspond to $m = 8, 9, 10, 11, 12, 13$, and 14 , respectively. The yellow vertical bands indicate the ELM-suppression/mitigation windows. The horizontal dotted lines indicate the top of the pedestal, $\Psi_N = 0.925$.

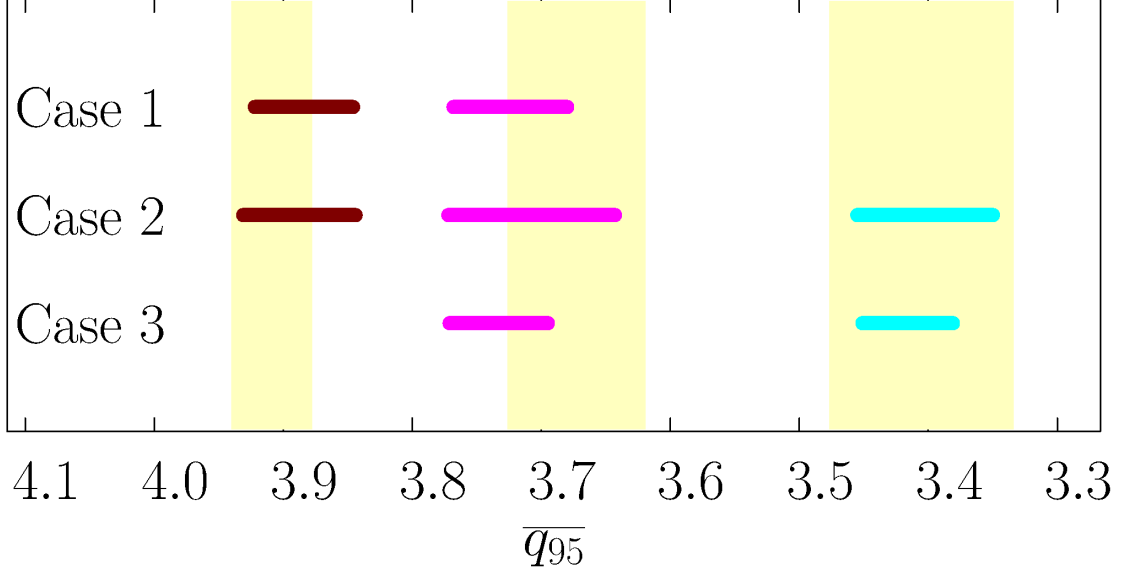


FIG. 14. Summary of results. The yellow vertical bands indicate the experimental $n = 3$ ELM-suppression/mitigation windows in DIII-D discharge #145380, as functions of the least-squares linear fit to q_{95} versus time. The brown, magenta, and cyan bars show the ELM suppression/mitigation windows predicted by the EPEC code that are associated with locked $m = 11/n = 3$, $10/3$, and $9/3$, magnetic island chains, respectively, driven at the top of the pedestal. The three cases considered are such that the natural frequency at a given resonant surface is determined by: 1) the local ion flow; 2) the local $\mathbf{E} \times \mathbf{B}$ velocity; 3) the local electron flow.